

Chapter 4: X-ray Imaging (Spectroscopic) Telescope

4.1. X-ray Telescope for the Overall Solar-C/Plan-B Science

In addition to its own scientific standpoint, the X-ray Imaging (Spectroscopic) Telescope shall have close scientific synergy with other Solar-C/Plan-B instruments to maximize outcome from the Solar-C observatory as a whole. While SUVIT and EUVS chiefly observe lower layers of solar atmosphere, the X-ray Imaging (Spectroscopic) Telescope observes the uppermost layer of the Sun, the corona, to achieve comprehensive understanding on magneto-hydrodynamic processes across the entire layers of solar atmosphere with various degrees of ionization. Science with Solar-C/Plan-B relevant to the corona shall address (a) forms and mechanisms of storage and dissipation of energy that was transferred upwards through photosphere and chromosphere, (b) quantitative understanding on the physics of magnetic reconnection which is believed to be the central engine for converting magnetic energy to thermal and kinetic energy of coronal plasmas, and possibly, (c) diagnostics on wave phenomena along magnetic field lines. Investigation of mechanism(s) for explosive energy release may also have relevance to space weather studies.

In pursuing such science capabilities, we consider the following two possibilities for the Solar-C/Plan-B X-ray Imaging Telescope:

- (1) Photon-counting imaging spectroscopy X-ray telescope
- (2) Ultra-high spatial resolution normal incidence EUV telescope

The photon-counting telescope adopts grazing-incidence optics and aims to perform imaging-spectroscopy of the soft X-ray corona from below 1 keV up to ~5 keV with its main scientific target being quantitative investigation of dissipation processes that act in the corona such as heating of active region corona and magnetic reconnection in flares. The upper-end of the energy range can be increased up to ~10 keV if we adopt a smaller grazing-incidence angle (~5 keV with 0.9 degrees while ~10 keV with 0.45 degrees) as will be described in the subsequent part of this report. The energy coverage up to ~10 keV will be particularly powerful in investigating heating and acceleration of plasmas in the reconnecting magnetic field structure in flares.

While the photon-counting telescope should be powerful in studying energy dissipation processes in the corona, it may have less overlap with the other Solar-C/Plan-B instruments (SUVIT and EUVS) in terms of temperature coverage (hence less overlap in the atmospheric layers of the Sun) and spatial resolution because of its grazing-incidence optics. Taking this point into account, the other possibility, the ultra-high spatial resolution normal incidence telescope has been considered. The normal incidence telescope puts its emphasis on delivering complementary observables for EUVS, providing context imagery information for EUVS with higher spatial

resolution than EUVS, with a wide field-of-view and with overlapping temperature coverage thus aims to investigate connection between transition region and the low corona.

4.2. Photon-Counting Imaging Spectroscopy X-ray Telescope

4.2.1. Scientific Objectives

The photon-counting imaging spectroscopy X-ray telescope will provide the first-ever opportunity to perform imaging-spectroscopic investigation of the corona in soft X-ray wavelength range, from below 1 keV up to ~5 keV (Figure 4.1).

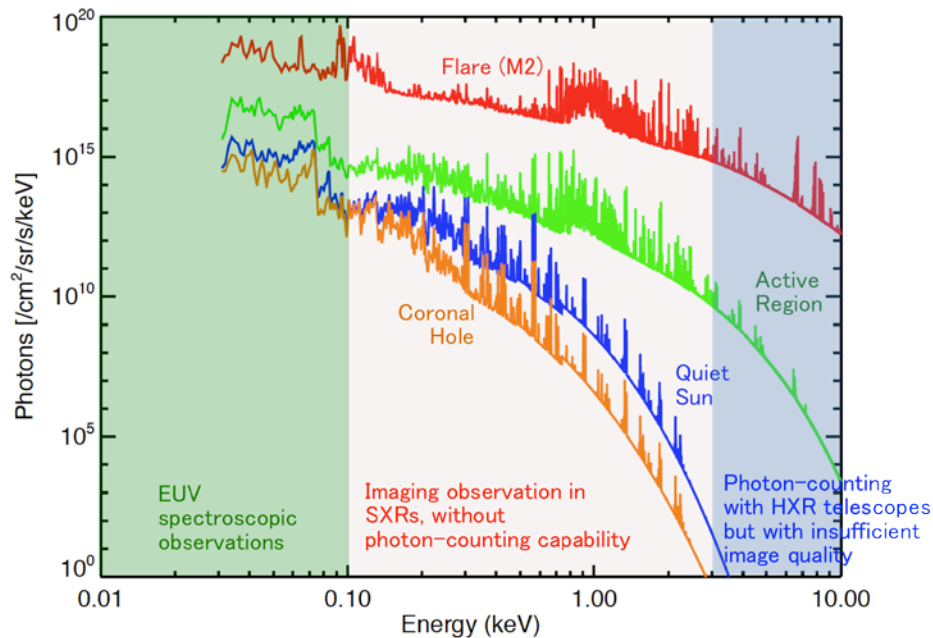


Figure 4.1. Status of past imaging-spectroscopic investigation in EUV/X-ray wavelengths overlaid with model solar spectra synthesized with CHIANTI Ver. 6. Imaging-spectroscopic investigation of the soft X-ray corona has so far remained totally unexplored.

Among Plan-B science goals detailed in Section 2, two main scientific targets of this telescope with photon-counting capability is summarized as follows:

- (1) *Quantitative investigation of structure and dynamics of magnetized plasmas around the site of magnetic reconnection.*

It is widely perceived, based on imaging observations with *Yohkoh*, that magnetic reconnection is the engine for liberating magnetic energy for plasma heating and particle acceleration in solar flares. Nevertheless, one has to say that understanding of the reconnection process, such as structures of slow and fast shocks, and temperatures and heating status of upstream and downstream plasma flows around the shocks, still

remains almost unclear. The most critical piece of information that has been missing to tackle this problem is spatially-resolved spectral information in the reconnecting magnetic structure. Previous X-ray telescopes (*Yohkoh* SXT and *Hinode* XRT) could only provide a single 'representative' temperature in the form of filter-ratio temperature which is more like a mean temperature weighted by the differential emission measure (DEM) distribution over the line-of-sight plasmas (Acton, Weston, and Bruner 1999). This feature of filter-ratio temperatures tends to smear out any spectral features across coronal structures unless the bulk of plasmas (namely, those with the largest fraction of DEM) changes its spectral shape. The photon-counting imaging-spectroscopy of reconnecting magnetic structure will characterize plasma status upstream and downstream of shock structures associated with magnetic reconnection. This would, in turn, identify location and structure of the reconnection shocks. Spectral information with low-scattering focusing optics for a variety of flares should provide key clues in quantitatively understanding the physics of magnetic reconnection.

While the photon-counting X-ray telescope can derive electron temperatures as the continuum Bremsstrahlung emission, emission-line diagnostic with EUVS can deliver information on ion temperatures. One remarkable possibility is that the combination of spatially-resolved electron and ion temperatures will provide us with significantly powerful tool for studying electron and ion heating especially in the downstream of the shocks.

(2) *Investigate temperature structure of active region corona, in particular that for high temperatures (above ~5 MK)*

One of the key information necessary for unravelling the mechanism(s) of coronal heating, in particular the hot corona around active regions, is to identify evolution of spectral structures together with their distribution across lateral (across active regions) or in vertical (height distribution) extents. This will enable one to locate site of heat input (hence dissipation site) across the area and subsequent heat flow that results in generating the hot corona. This approach may be particularly effective if the heating is intermittent (*i.e.*, by nano-flares). The non-dispersive nature of photon-counting imaging-spectroscopy, in contrast to dispersive, scanning, instruments will be effective in identifying such heat input and subsequent flow in the corona by measuring spectral evolution taken simultaneously across a wide field-of-view. Instruments that utilize EUV wavelengths may not be suitable for this investigation due to lack of strong EUV emission lines at high temperatures from active regions.

Discovery space with imaging spectroscopy of an extended energy range

In this report, the X-ray grazing-incidence angle to the mirror of 0.9 degrees set as the baseline. While this grazing-incidence angle provides certain capability for performing imaging-spectroscopic observations of active regions (see below for details), the highest energy available for flare observations would be limited to ~5 keV (Figure 4.13). An interesting possibility which greatly enhances observation capability for flares, with decreased capability for active regions, is to go to an even smaller incidence angle. For example, the grazing-incidence angle of 0.45 degrees will increase the highest energy

available for flare observations to as high as ~ 10 keV (Figure 4.14).

The small incidence angle (*e.g.*, 0.45 degrees) for the photon-counting telescope will enable imaging spectroscopy in the energy range of a few to ~ 10 keV. This performance provides the following discovery space for flare sciences in the field of reconnection study:

(1a) Identification of high-temperature plasmas in the flaring magnetic field structure

The increase in the energy range up to ~ 10 keV will enable one to observe Fe (~ 6.7 keV) and Fe/Ni (~ 8 keV) line complexes together with thermal-bremsstrahlung continuum from high temperature plasmas in energy spectra of flares. When combined with the expected imaging-spectroscopic performance of the telescope shown in Figure 4.15, this means that we'll be able to track spatial distribution and its evolution of super-hot ($> \sim 30$ MK) plasmas with angular scale and temporal resolution combination of 2" with every 5 s (or 1" with every 20 s). Imaging spectroscopy with such fine spatial scale and temporal resolution will enable us to identify site of in-situ heating and to discuss heating of plasmas in the reconnecting magnetic field structure.

(1b) Evolution of non-thermal (or supra-thermal) electron population

The extended energy coverage should also provide breakthrough in understanding particle acceleration mechanism(s) in solar flares. It is generally believed that initial particle acceleration takes place inside the reconnection region (forming reconnection outflows), followed by transport to and further acceleration somewhere at the outer part of it (see Tsuneta & Naito (1998) for the case of fast-shock acceleration). However, it has so far remained unclear, or even unexplored, where and how particles (ions and electrons) are accelerated in the reconnecting structure. While soft X-ray imaging-spectroscopy of the reconnecting magnetic structure should naturally be powerful in identifying, and tracing the evolution of, *e.g.*, shock structures associated with magnetic reconnection, observations with the extended energy range of up to ~ 10 keV (as compared to ~ 5 keV in the baseline design) would provide enormous leap in unravelling the nature of particle acceleration in flares. This is because the observations will deliver information on how and where supra-thermal electron distributions (manifest themselves as power-law X-ray spectra) grow out of the ambient thermal electron distribution, especially near the onset of particle acceleration where soft X-ray emission from thermal plasmas along the line of sight is yet to be dominated. As the mean energy of thermal electrons is typically 2-3 keV, X-ray emission by supra-thermal electrons can be well identified in the ~ 5 -10 keV range. Note there has been a number of observations reported since 1980's that non-thermal X-ray emission from flares may extend down below 10 keV. Furthermore, there is related observational support from in situ observations of the Earth's magnetosphere that supra-thermal electrons appear in energy spectra around 4 times as large as thermal energy (2 keV) near the reconnection region (see, *e.g.*, Imada et al. 2007). Thus, the extended energy coverage, coupled with high dynamic-range imagery with soft X-ray focusing optics, will give us a unique opportunity to locate the site of electron acceleration and to study the nature of the acceleration in relationship with the reconnecting magnetic field structures such as

shocks.

Table 4.1. Key parameters of the photon-counting X-ray telescope.

Item	Description	Remarks
Overall description	Perform imaging investigation of the X-ray corona with the following two modes. Two modes selectable (not simultaneously). (1) Photon-counting mode: Imaging spectroscopy for a limited region of interest. (2) Photon-integration mode: Imagery with the entire, or part of, the imaging array. Walter Type I (-like) grazing-incidence telescope with a segment mirror. A CMOS-APS detector to be used as the focal-plane imaging array.	
Envelope dimensions of the telescope	~40cm × 40cm × 4.5m (TBD)	Telescope plus the focal-plane camera. Includes housings.
Angular resolution & Temporal resolution for photon counting	For photon-integration mode: ~1" (~0.5"/pixel) For photon-counting mode: For active regions and flares, generate an X-ray spectrum for spatial area whose size* ~< 2"×2" (goal) / ~4"×4" (min.) within every < 10 s (goal) / 30 s (min.)	* Spatial area size in which a spectrum with good counting statistics can be synthesized with reasonable integration time.
Field of view	For photon-integration mode*: ~13'×13' For photon-counting mode**: >~3'×3' (goal) ~80"×80" (nom.) ~40"×40" (min.) 'Elongated' FOV (such as ~40"×13') is possible	* Off-axis image blur not taken into account. ** Area with which photon-counting analysis can be performed.
Energy range	~0.5-5 keV* (baseline) ~0.5~10 keV* (under study)	* Energy range above 2 keV available during flares, with photon-counting mode.
Energy resolution	ΔE (FWHM)*: ~130 eV (goal), 150 eV (nom.) @ 5.9 keV ~74 eV (goal) @ 1.5 keV Readout noise: ~43 eV FWHM (goal)	* Includes readout noise.
Data rate	(With the event processing in Section 6.2.3.4) max. 110 Mbps for 512×512 photon-counting area max. 6.9 Mbps for 128×128 photon-counting area	No data compression assumed. For 10-bits A/D conversion.
Pre-filter	Same as Hinode/XRT.	Entrance filter for rejecting visible light and heat input to the telescope.
Visible-light optics	TBD	
X-ray flux monitor	TBD; for controlling X-ray flux attenuation filters.	

Besides photon-counting capability, the telescope will also be capable of providing images of soft X-ray corona (with conventional photon-integration, or 'flux mode') with the highest angular resolution of 1 arcsec (0.5 arcsec pixel size) as a solar X-ray imager. Such images will deliver context information for other Plan-B instruments.

By adopting an X-ray CMOS active-pixel sensor (APS) device for the focal-plane imaging array, the photon-counting X-ray telescope will be free from "spill-over" of signal charges for over-exposed images which is often seen with soft X-ray imagers employing CCDs without anti-blooming pixel architecture, including *Hinode* XRT and *Yohkoh* SXT. The spill-over-free feature of the telescope, combined with high dynamic-range focusing optics imagery, should be particularly powerful for the soft X-ray corona, in detecting faint features that could be present right next to a bright feature, such as material flows and ejecta associated with magnetic reconnection.

With the advent of recent progress in high-speed, low noise, CMOS-APS detectors, the photon-counting X-ray telescope for Solar-C/Plan-B should provide breakthrough in our understanding on energy storage and dissipation in the corona, including the physics of magnetic reconnection. Key parameters of the photon-counting telescope are given in Table 4.1.

4.2.2 Required Specification for the Instrument

4.2.2.1 Optics

Photon-counting imagery in X-rays needs be done with grazing-incidence optics that can cover, continuously, a wide spectral range of X-ray emission from the corona. Normal-incidence imagers may not be suitable for the photon-counting purpose because (1) they can image only a narrow wavelength range for each passband, and (2) since the wavelengths for normal-incidence imagers are in the EUV range whose photon energies below ~ 100 eV, silicon detectors such as CMOS-APS, whose best-expected FWHM energy resolution would be around ~ 50 eV at those energies, are not sufficient for resolving fine spectral features in the EUV range. A grazing incidence telescope is chosen to utilize the sensitivity to the hotter plasmas and the associated spectral lines, in soft X-rays.

4.2.2.2 Angular Resolution

It has been suggested by recent *Hinode* EIS observations (Hara *et al.* 2008) that sub-arcsecond structures in coronal loops may be important in understanding elementary processes of coronal heating for active regions. In this regard, pixel size of less than 1", say, 0.5", would be preferable for photon-integration imagery. For photon-counting imaging spectroscopy, while angular resolution of, *e.g.*, 5" (that is, energy spectra with every 5" square; half-resolution pixel size of *Yohkoh* SXT) could still provide new spectroscopic information on the hot corona, especially for large magnetic structures such as reconnecting loop structure seen in long-duration flares (LDEs), higher angular resolution even beyond that (*e.g.*, 2" square or even higher) would be much desired in investigating spectral features in active region loops and in

reconnecting magnetic structures in flares.

4.2.2.3 Temporal Resolution / Cadence

From photon counting viewpoint, capability of generating an energy spectrum every 30 s or shorter should be necessary for active regions to see their thermal evolution. For flares, temporal resolution for generating energy spectra of 10 s, or shorter, should be desired.

4.2.2.4 Energy Range and Energy Resolution

Imaging-spectroscopic capability for hot corona should be essential for investigating flare science such as reconnecting structures. This leads to a requirement that the telescope should be sensitive beyond 2 keV (which is the upper limit for *Hinode* XRT), to several keV's. Also, sensitivity below 1 keV is desired for imagery with photon integration to image quiet Sun and coronal holes. Regarding energy resolution for photon-counting observations, FWHM resolution of ~150 eV is needed to observe higher end of the energy range (several keV's). For low-energy range of around 1 keV, necessary energy resolution is currently under investigation. As is discussed in Section 4.2.4, a combination of 5 electrons (rms) read-out noise and Fano-limited energy resolution (with Fano factor $F = 0.12$ for silicon) provides comfortable energy resolution for observing emission lines in the ~1 to 2 keV range.

4.2.3 Baseline Instrumentation

4.2.3.1 Overview

In response to specifications based on scientific requirements, we propose a photon-counting soft X-ray telescope whose observational performance summarized in Table 4.1. In this Section, we explain key items for the proposed telescope.

(a) Optics System

Figure 4.2 indicates a preliminary sketch of the grazing-incidence telescope with photon-counting capability. The telescope consists of (1) a pre-filter in front of the entrance aperture, (2) front-end grazing-incidence mirror of Walter Type I (-like) design, (3) focal-plane CMOS image sensor, (4) analysis/attenuation filters in front of the CMOS detector, (5) focal-plane shutter, and (6) camera control & event processing electronics (items (1), (5) and (6) not shown in Figure 4.2). There may be an aperture adjustment mechanism under consideration that is to be mounted in front of the telescope aperture to reduce incident flux to an appropriate level when performing photon-counting observations. The telescope will have ~4 m of focal length.

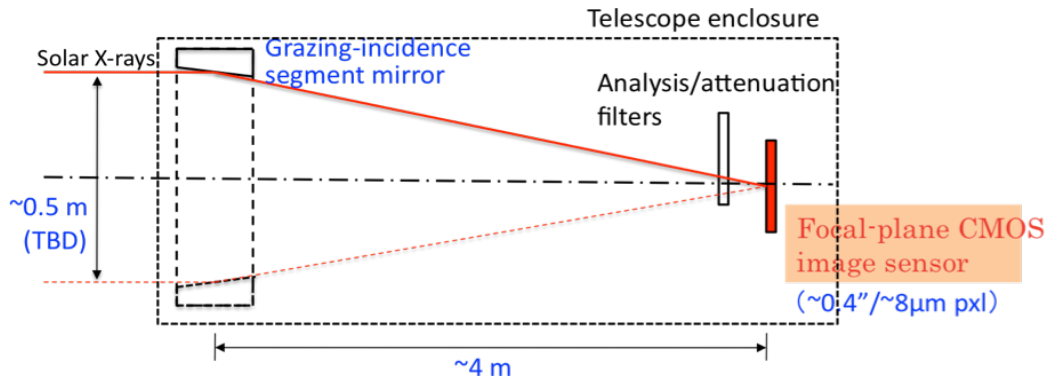


Figure 4.2. Schematic illustration of a preliminary photon-counting telescope concept.

(b) Event Processing System

In addition to the optical performance of the grazing-incidence mirror, accurate measurement of energy and position on the detector for each detected photon, with avoiding significant pulse pile-up effect, is a crucial key for the success of this instrument. Figure 4.3 presents a preliminary diagram for event processing under photon-counting measurement.

Besides the function blocks indicated in Figure 4.3, the telescope should employ appropriate attenuation filter or aperture size in response to the incident flux level.

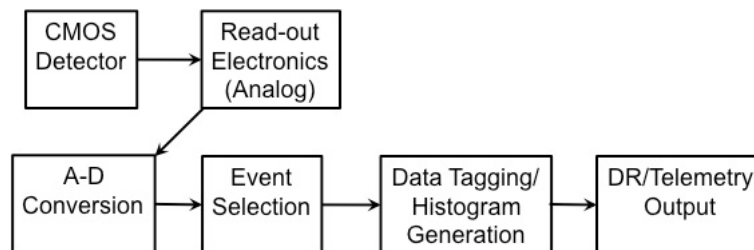


Figure 4.3. A preliminary block diagram describing the event processing scheme for detected X-ray photons under photon-counting measurement.

4.2.3.2 Optics/Mirror

A piece of grazing-incidence segment mirror, consisting of 1/8 of an entire circle, will be adopted for the X-ray mirror of the telescope. The mirror employs a Walter-I (-like) design with 2 reflections, with the length (in optics axis direction) of the first reflection segment designed to be 40 mm (TBD). While the radius of the mirror r (radius of an entire circle along which the segment mirror is laid), located at $f = 4$ m in front of the detector, changes with different grazing incidence angle to the mirror θ_i with the following relation

$$r = f \times 4\theta_i ,$$

we take $\theta_i = 0.9$ degrees as the baseline to perform imaging-spectroscopy both for active regions and flares. Grazing angles of 0.45, 1.35, and 1.8 degrees have also been studied. Besides the baseline incidence angle, $\theta_i = 0.45$ degrees could be an interesting option for flare sciences (Section 4.2.4.3) but with penalty of poor observational performance for active regions. The baseline diameter of the mirror with the grazing incidence angle of 0.9 degrees is 50.3 cm.

Unlike *Hinode* XRT, the mirror must be coated with iridium (Ir) to attain high reflectivity, hence sensitivity of the telescope, for keV X-rays.

A conceptual schematics of the segment mirror mount is shown in Figure 4.4, with a drawing for the mirror-detector package in Figure 4.5.

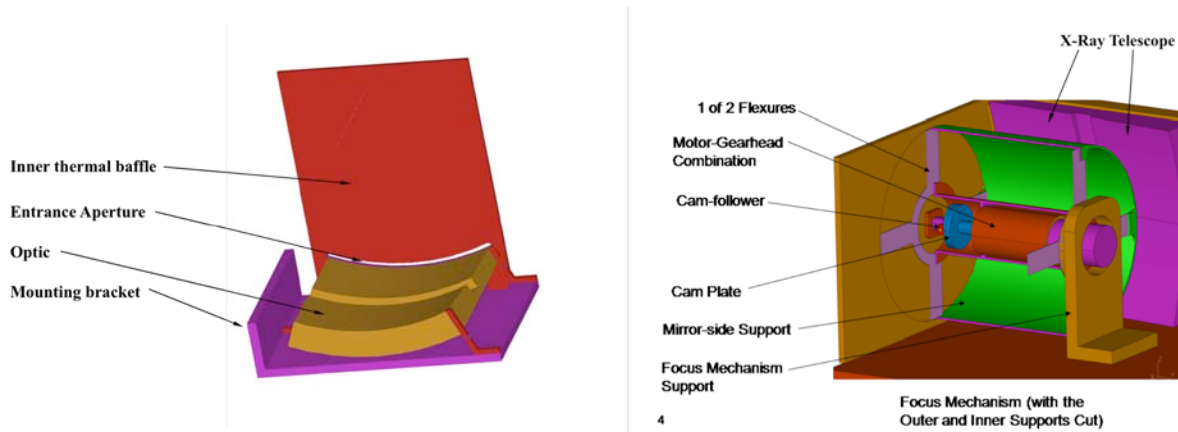


Figure 4.4. *Left:* Close-up of a segment mirror unit consisting of primary and secondary reflecting surfaces, having 1/8 segment of the entire circle. *Right:* Preliminary conceptual illustration on the focus mechanism which moves the mirror segment along the direction of the optics axis.

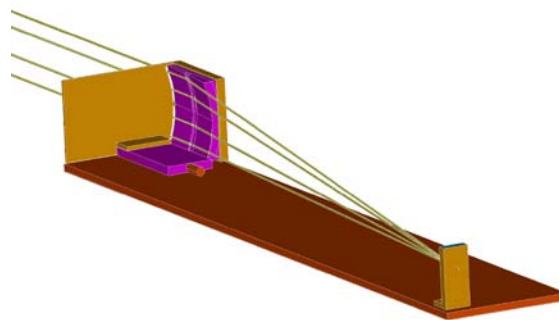


Figure 4.5. An illustration indicating segment mirror unit (left) and the focal-plane detector (right). Ray paths for X-rays from the Sun also shown in the figure.

A preliminary set of baseline parameters for the X-ray mirror is summarized in Table 4.2. A key requirement to the grazing-incidence mirror is that it should keep very small figure error (deviation from ideal mirror surface profile) to achieve 1 arcsec resolution (0.5 arcsec pixel size) while maintaining small micro-roughness for suppressing X-ray

scattering from other (bright) features on the Sun. A first-cut, rough estimate indicates that the figure error of ~ 10 nm P-V (TBD) would be needed to have Half-Power Diameter of 0.5 arcsec for angular resolution and micro-roughness of 3-4 Å r.m.s. (TBD) to suppress off-axis scattering wing level down to $\sim 10^{-5}$ of the core at 1 arcmin off-axis at Al-K.

While fabrication of a mirror with the above specification is challenging, development of the mirror with Japanese domestic partners is currently under investigation which might provide possible solution for the fabrication.

Table 4.2. Baseline parameters for the X-ray mirror (preliminary).

Item	Description	Remarks
Mirror type	Walter Type I (-like) grazing incidence mirror, with two reflections at the primary and the secondary reflection segments.	
Length of the reflection segment	40 mm for the primary reflection segment. TBD mm (~ 50 mm) for the secondary reflection segment.	TBD; May be increased depending on tolerance for aberration.
Annular segment profile	1/8 of the entire circle.	
Grazing incidence angle	0.9 degrees	Baseline value.
Annular radius of curvature	251.3 mm	For grazing-incidence angle of 0.9 degrees.
Mirror surface	Coated with iridium (Ir)	Coating is a must for science performance of the telescope.
Focal length	4.0 m	
Plate scale	0.41"/8 μ m (0.5"/10 μ m)	8-10 μ m corresponds to the pixel size of the baseline detector.
Angular resolution performance		
Core	Figure error of the mirror ~ 10 nm P-V (TBD) to have 0.5 arcsec HPD (Half-Power Diameter).	
Wing	Mirror micro-roughness 3-4 Å r.m.s. (TBD) to sufficiently suppress off-axis scattering wing level down to $\sim 10^{-5}$ of the core at 1-arcmin off-axis at Al-K.	

4.2.3.3 Focal-Plane Detector

Table 4.3 summarizes baseline specifications for the focal-plane detector to meet the instrument performance tabulated in Table 4.1. In order to achieve high frame readout at the focal-plane detector, we identify CMOS image sensors as the most appropriate for our purpose. There are several active-pixel detectors under development besides CMOS which aim pixel-based spectroscopy on X-ray photons, such as DEPFET for *IXO* X-ray observatory (former *XEUS*; Strüder *et al.* 2003, 2004, Treis *et al.* 2005, Strüder 2008) and pixel detectors for high-energy particle accelerator applications such as for LHC

(e.g., Llopart *et al.* 2007), these detectors mostly have large pixel size of typically $\sim 50 \mu\text{m}$, with the smallest one at most $\sim 25 \mu\text{m}$. The large pixel size of these detectors, unfortunately, is not consistent with the required angular size of a pixel of $\sim 0.5''$ unless the telescope has significantly large focal length exceeding 10 m.

Recently, there has been remarkable development in CMOS active-pixel image sensors which appear to be best suited as our photon-counting detector because of their small pixel size (can easily be smaller than $10 \mu\text{m}$) and their potential of high frame readout capability.

Table 4.3. Baseline specification for the focal-plane detector (preliminary).

Item	Description	Remarks
Device type	CMOS-APS	Device from e2v considered to be the baseline.
Format	2k×2k or larger	
Pixel size	8-10 μm	
Photon-counting area	512×512 (goal) 100×100 (minimum)	Should be changeable over the imaging area.
Frame readout rate for photon counting	1000 fps	
Pixel gain	>a few $\times 10$ (>50) $\mu\text{V}/e^-$ for photon-counting pixels a few $\mu\text{V}/e^-$ for photon-integration pixels	Should be switchable over the imaging area.
Low-energy X-ray sensitivity	Back-illuminated device, or thin ($\sim <1 \mu\text{m}$) SiO_2 absorption layer if a front-illuminated device is employed.	
Readout noise	5 e^- rms (TBD; goal) ≤ 50 eV FWHM (minimum)	
Energy resolution	Fano-limited ($F=0.12$) (goal) ≤ 150 eV FWHM (minimum)	
Charge spreading	At least 3- σ electron cloud diameter smaller than 3 pixels.	
Pulse-height A/D conversion	≥ 10 bits	

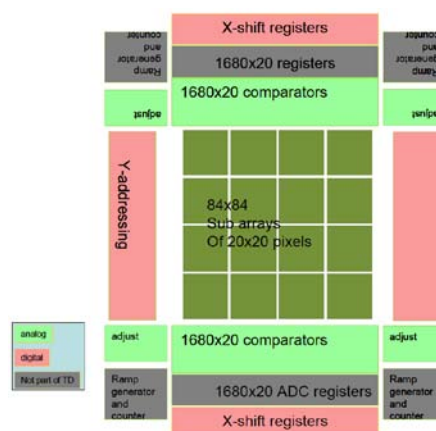


Figure 4.6. Envisaged CMOS-APS for WFS whose development ongoing at e2v. An area of 1680×1680 pixels is planned to be read out with a frame rate of 700 fps (nominal) and with readout noise of $\sim 3 e^-$ r.m.s. Figure courtesy of e2v.

As of this writing, the most promising series of devices along the line of our need is those which could be provided by e2v Technologies, U.K. A large-format wavefront sensor (WFS) for night astronomy is currently under development by e2v (Figure 4.6). The target specification for the WFS is to read out $1.6\text{k} \times 1.6\text{k}$ pixels ($24\ \mu\text{m}$ pixel size) area at a frame rate of 700 fps (nominal) with low readout noise (a few e^- r.m.s.), backside illumination with bulk depletion using high-resistivity epitaxial silicon. They have recently successfully completed demonstration of their approach on pixel architecture to achieve low readout noise together with high frame rate, and are now quite confident that most, if not all (except the largest case of the photon-counting area), of baseline specifications in Table 4.3 can be met with their pixel architecture developed for the WFS. Figure 4.7 depicts possible readout of the photon-counting area among the $2\text{k} \times 2\text{k}$ imaging area (pixel size 8-10 μm) based on the existing architecture at e2v with the background of WFS heritage. Final pixel size will be determined considering effect of charge spreading by X-ray photons on event detection efficiency.

The extended readout area in the horizontal direction in the figure would be particularly effective when considering the possibility of flexible spacecraft roll to be mentioned in Chapter 5 in such a way that the horizontally-extended area can serve as a vertical 'slit' along which imaging spectroscopy can be performed.

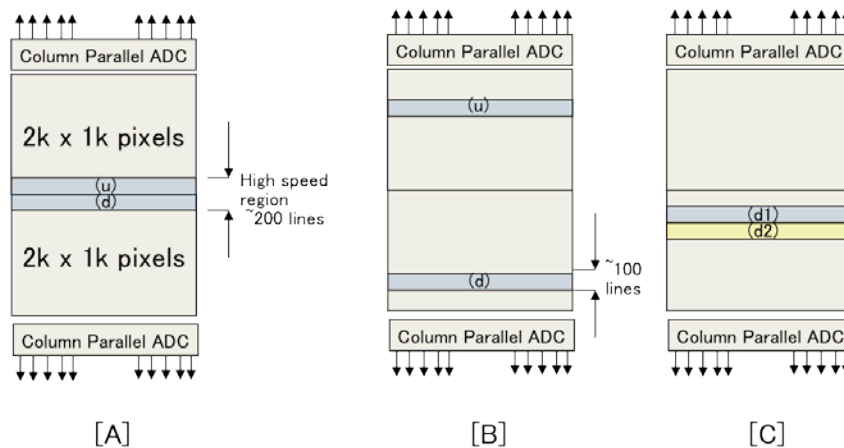


Figure 4.7. Possible readout scheme of photon-counting area in the $2\text{k} \times 2\text{k}$ array with the existing pixel architecture at e2v. In the figure, areas labelled as '(u)' are read out from the upper side of the detector while those with '(d)' from the lower side, each with 1000 fps. [A] $2\text{k} \times 200$ area in the middle of the imaging area to be read out with 1000 fps. [B] Two separate $2\text{k} \times 100$ areas to be read out. [C] Switch read out of area (d1) and (d2) each other so that a total of $2\text{k} \times 200$ area in the lower half of the detector be read out at 500 fps, which may be useful for observing weak sources extending large spatial extent. Figure courtesy of e2v.

In parallel to the development of high frame-rate readout, back-thinning of CMOS-APS is also being extensively promoted at e2v, using high resistivity ($\sim 1\ \text{k}\Omega\text{-cm}$) epitaxial silicon to have the bulk silicon depleted instead of depleting only a limited portion around the p-n junction of the photo-diode in each pixel thus attaining a depletion layer thickness of $\sim 10\ \mu\text{m}$ or even more. A sample of such back-thinned CMOS-APS is said to become commercially available next year (2011). A prototype WFS device with $\sim 800 \times 600$ pixels and with a readout rate of 700 fps (1000 fps max.)

for the entire area is scheduled to appear in 2012, again with back-thinning and with high-resistivity silicon.

As for spreading of signal charges by incident X-ray photons, only limited results have so far been available with e2v CMOS-APS devices. Nonetheless, results from X-ray illumination with Mn target (that emits Mn $K\alpha$ and $K\beta$ lines besides Bremsstrahlung continuum) for a front-illuminated device performed at Centre for Electronic Imaging at The Open University indicates the X-ray signals are contained within 3×3 pixels area with $\sim 20\%$ of Mn $K\alpha$ (5.9 keV) events resulting in single-pixel events even with a small pixel size of $5.8\ \mu\text{m}$ and with low resistivity silicon (hence shallow depletion layer). This result suggests promising prospects that the extent of charge spreading (and also fraction of single-pixel events) would even be better with a larger pixel size of $8\text{-}10\ \mu\text{m}$ and with high resistivity silicon.

To summarize, at this very moment there is no CMOS-APS device present that immediately meets the baseline specifications for the photon counting. However, with the rapid development of CMOS-APS currently ongoing towards the desired direction of (1) high-speed and low-noise readout capability and (2) good soft X-ray spectroscopic capability, the photon-counting detector is expected to become even more realistic within the upcoming 1-2 years.

In the subsequent section of this Report, we assume back-illuminated CMOS device from e2v, with $10\ \mu\text{m}$ -thick depletion layer and with $8\ \mu\text{m}$ pixel size for assessing science capability of the photon-counting telescope.

4.2.3.4 Flux Attenuation System

For performing photon-counting observations for flares and active regions, it is deemed necessary to employ attenuation system for the incident X-ray flux so as to avoid event pile-up on the focal-plane detector. Either a set of attenuation filters mounted on a filter wheel(s) or an aperture adjustment mechanism would be employed for the flux attenuation system with the former may be more suited to observe higher end of the spectrum because the attenuation filters absorb lower-energy X-ray photons. While logic for selecting certain attenuation filter or a particular aperture size (with probably using signals from a separate flux monitor) needs be elaborated, observations with the baseline geo-stationary orbit (see Section 5) could provide a remarkable chance of performing such attenuation on true real-time basis.

4.2.4 Expected Capability

4.2.4.1 Introduction

Figure 4.8 shows effective area profiles of the telescope for the four grazing-incidence angles θ_i studied ($\theta_i = 0.45, 0.9, 1.35,$ and 1.8 degrees), with $\theta_i = 0.9$ degrees being considered as the baseline. The effective area profiles include (1) X-ray transmission of the pre-filter (same material design as *Hinode* XRT, namely, $1200\ \text{\AA}$ of

aluminum on 2500 Å polyimide assumed), (2) reflectivity of the grazing-incidence mirror, (3) projected QE of the focal-plane CMOS detector, and (4) geometrical area of the telescope that is determined by the aperture size of the first reflecting segment of the mirror, when viewed from the Sun.

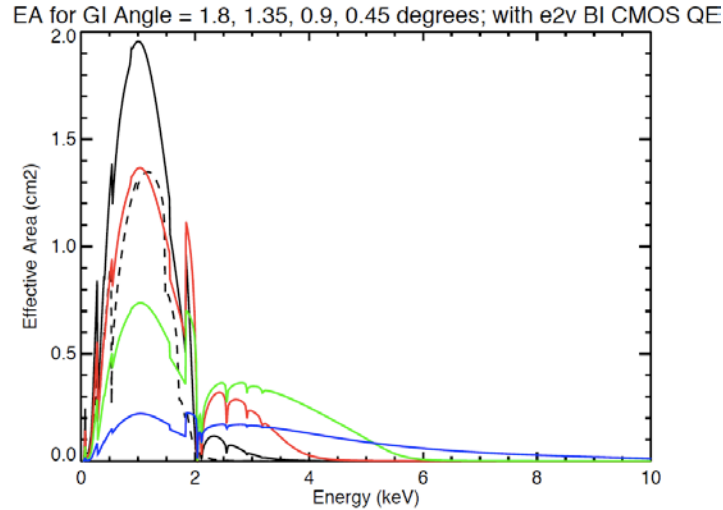


Figure 4.8. Effective area profiles for grazing incidence angles of 1.8 (black), 1.35 (red), 0.9 (green), and 0.45 (blue) degrees. The effective area profile for Hinode XRT (without Ir coating on the mirror surface) is also shown for comparison (black dashed line). QE profile for the back-illuminated e2v CMOS device assumed for all the four grazing incidence angle profiles.

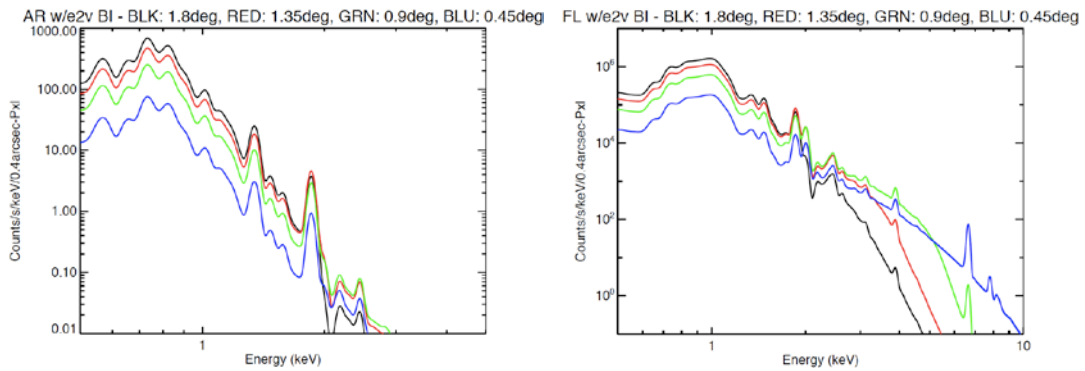


Figure 4.9. *Left*: X-ray count spectra for a model active region with CHIANTI V6.0, for four grazing-incidence angles, 1.8, 1.35, 0.9, and 0.45 degrees (in black, red, green, and blue, respectively). No attenuation filters assumed to be present. *Right*: Those for a model flare (GOES class M2). Again without attenuation filters.

Figure 4.9 indicates X-ray count spectra for a model active region (left panel) and a model flare (right panel) from CHIANTI V6.0 (Dere *et al.* 2009), without focal-plane filters. Readout noise and energy resolution indicated as "goal" in Table 6.2-4 are used for generating these plots. Note with the back-illuminated CMOS neither active region nor flare count spectra can be observed as they are in the photon-counting mode because incident X-ray count rates will be too high (*e.g.*, in the flare case, $\sim 3 \times 10^5$ cts/s/pixel for $\theta_i = 0.9$ deg.) to perform any meaningful photon counting avoiding pulse

pile-up. For this reason, focal-plane attenuation filters should be necessary. The attenuation filters will make count spectra to be actually measured different from those in Figure 4.9, with low-keV portion to be significantly attenuated. In the photon-integration mode, such attenuation filters will not be necessary but analysis filters for performing filter-ratio analysis may be employed.

Signal count rates to the focal-plane detector of the telescope without attenuation filters (nor focal-plane analysis filters) is summarized in Table 4.4. Here, the baseline back-illuminated CMOS detector is assumed for estimating signal count rates.

Table 4.4. Estimated signal count rate for the telescope, with the baseline detector and the grazing-incidence angle of 0.9° .

Target ⁽¹⁾	Flare (M2)	Active Region	Quiet Sun	Coronal Hole
Photon count rate (cts/s/pxl)	3.1×10^5 ⁽²⁾	2.2×10^2 ⁽²⁾	7.9	1.7
Electron rate (e ⁻ /s/pxl)	7.4×10^7	1.8×10^4	1.9×10^2	3.5×10^1
Exposure time for photon-integration ⁽³⁾	1.0 ms	4.2 s	3.9×10^2 s	2.1×10^3 s

(1) Emission spectrum from each target created from CHIANTI V6.0.

(2) Attenuation filters (and/or aperture adjuster) need be inserted in order to perform photon-counting spectroscopy.

(3) Time for generating 75 ke⁻, which is half the nominal full-well capacity of the CCD for *Hinode* XRT.

4.2.4.2 Active Regions

Figure 4.10 presents simulated photon count spectra to be detected with the photon-counting mode of the telescope, with the baseline grazing-incidence angle of $\theta_i = 0.9$ degrees. A model DEM for active region (Vernazza and Reeves 1978) with CHIANTI V6.0 emission code is used for obtaining solar emission from a "typical" active region. The spectra assumes 1024 energy bins between 30 eV to 10 keV, with binning made in such a way that count rate from each summed-bin has at least $5\text{-}\sigma$ statistical significance against Poisson errors (only photon counts are considered here as the source of the error), with an imposed limitation that the maximum number of binning be 20. A set of readout noise of 5 electrons r.m.s. and Fano-limited energy resolution (with Fano factor $F = 0.12$) is adopted here to produce the spectra. This set of readout noise and energy resolution is listed as goal for the detector specification in Table 4.3.

Left panel of Figure 4.10 shows a spectrum with 262 s net integration time while the right panel 654 s net integration. Here, net integration time stands for the total of integration time from each pixel that contributes for generating a single energy spectrum. For example, for generating the left-side spectrum of the figure, it will take 16 s with 4×4 pixels (1.6" square).

As seen in the figure, an emission line complex of Mg may be detected around 1.34 keV even with the 262 s net integration case with positive, or marginal, indication of another emission line complex of Si around 1.85 keV. As the contribution curves for these emission line complexes peak at 5-8 MK, any deviation of measured emission line complexes from Figure 4.10 immediately give us information on distribution and

evolution of high-temperature (≥ 5 MK) plasmas that has never been provided before.

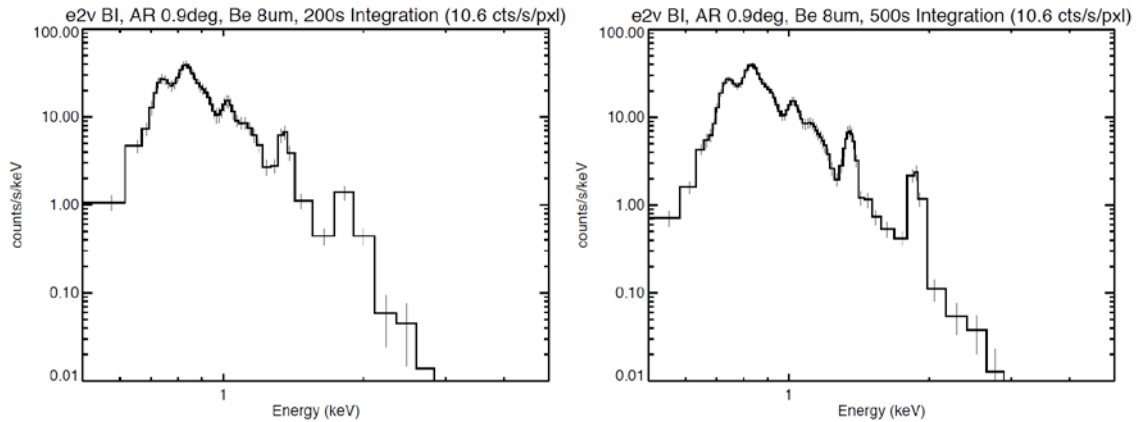


Figure 4.10. Simulated photon count spectra for a "typical" active region with the baseline grazing-incidence angle of 0.9 degrees and with the baseline CMOS detector. *Left*: With net integration time of 262 s. *Right*: Net integration time 654 s.

If we concentrate on the low-temperature emission in the energy range below ~ 1 keV, energy spectra in that energy range can be generated even quickly. Figure 4.11 shows an example of active region spectrum with 2 μm -thick Be filter employed as the attenuation filter (yielding incident photon count rate of 39.1 counts/s/pixel to the detector) with net integration time of 130 s. This means the spectrum in the figure would be obtained every 14 s with 3×3 pixels (1.2" square).

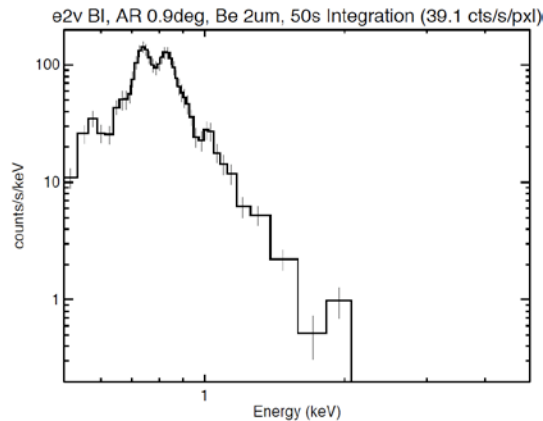


Figure 4.11. Simulated photon count spectra for a "typical" active region with the baseline grazing-incidence angle of 0.9 degrees and with the baseline CMOS detector, with net integration time of 130 s.

Apart from thermal emission so far studied, if non-thermal emission were to extend down to, say a few keV range, at the early phase of a flare, such non-thermal emission is likely to be well detected as continuum component in the spectra, in a spatially-revolved way. Note detection of such non-thermal components would not be available with EUV spectrographs since they manifest themselves as continuum emission, and can be done only with the X-ray imaging-spectroscopic approach. So far, spatially-resolved observations of non-thermal components down to a few-keV range have not been performed except for very limited cases (Krucker *et al.* 2002, Hannah *et al.* 2008).

Observations with the photon-counting X-ray telescope will provide crucial information on physical condition of the corona that triggers explosive energy release in flares.

4.2.4.3 Flares

In the case of flares (with a model flare of GOES class M2 studied with CHIANTI spectral code), attenuation filters are necessary to reduce incident rate of X-ray photons to the detector in order to avoid excess photon pile-up, down to a level of several times 10 photons/s/pixel. Energy spectra thus observed will therefore undergo significant attenuation of low-keV energy components by the attenuation filters. Figure 4.12 shows expected photon count spectrum profiles for a model flare of GOES M2 class to be detected with the photon-counting mode of the telescope, for different grazing-incidence angles, with an attenuation filter (beryllium assumed) inserted in each case to reduce the incident photon count rate down to ~ 40 photons/s/pixel. As seen in the figure, peak position of the spectrum changes with different grazing-incidence angles. Note in actual observations (with limited integration time for a spectrum) count rates down to roughly 2 orders of magnitude lower than the peak would give a practical lower limit for meaningful spectra with good, or reasonable, photon statistics. Hence energy range that can be explored differs with different grazing-incident angles.

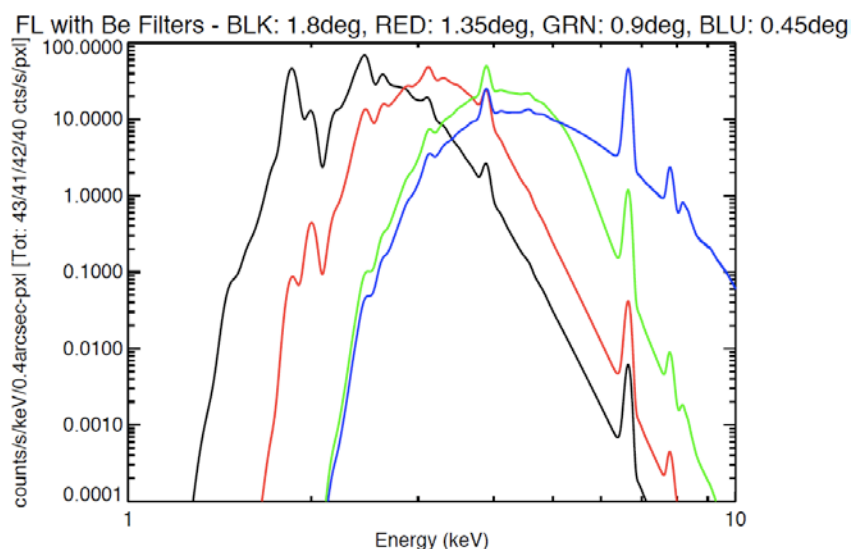


Figure 4.12. Photon count spectrum profiles expected from a model GOES M2 flare for the four different grazing-incident angles. An attenuation filter made of beryllium assumed for each profile; thickness 0.42 mm for $\theta_i = 1.8^\circ$, 0.8 mm for $\theta_i = 1.35^\circ$, 1.5 mm for $\theta_i = 0.9^\circ$, and 1.5 mm for $\theta_i = 0.45^\circ$ so that each spectrum has a similar total count rate of ~ 40 counts/s/pixel. Note the profiles are ideal ones with infinitely-good photon statistics.

Figure 4.13 presents simulated photon count spectra with the photon-counting mode of the telescope, with the baseline grazing-incidence angle of $\theta_i = 0.9$ degrees. A focal-plane attenuation filter of 1.5 mm-thick beryllium is inserted to reduce incident count rate down to 42.3 counts/s/pixel. A model DEM for a GOES M2-class flare (Dere and Cook, 1979) with CHIANTI V6.0 emission code is used for obtaining solar

emission for this flare case. For displaying flare count spectra, binning was made so that count rate from each summed-bin has at least $10\text{-}\sigma$ statistical significance against Poisson errors (only photon counts are considered here as the source of the error), with the maximum number of binning set to be 20. The left panel of the figure corresponds to 140 s net integration while the right panel 840 s. Even with the 140 s net integration time (that means 15.6 s integration for a $1.2''\times 1.2''$ area (3×3 pixels)), signature of Ca XIX emission (emission from 20 MK plasma) at ~ 3.9 keV can be seen in addition to the continuum thermal emission. Note these spectra only reflect thermal emission from flare plasmas; any non-thermal emission, if present, can be overlapped to these spectra.

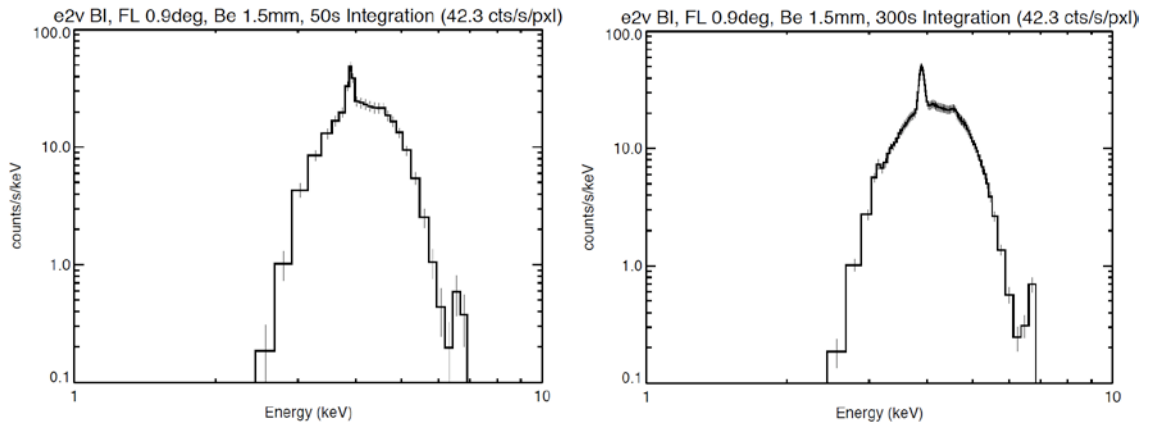


Figure 4.13. Simulated photon count spectra for a model flare of GOES M2 class with the photon-counting mode of the telescope of $\theta_i = 0.9^\circ$. *Left*: Net integration time 140 s. *Right*: Net integration time 840 s.

As supplementary information, Figure 4.14 shows simulated flare spectra with grazing-incidence angle of $\theta_i = 0.45$ degrees. This grazing angle could provide an interesting possibility that, in addition to the Ca XIX emission Fe and Fe/Ni emission complexes around 6.7 keV and 8 keV, respectively, may also be detected.

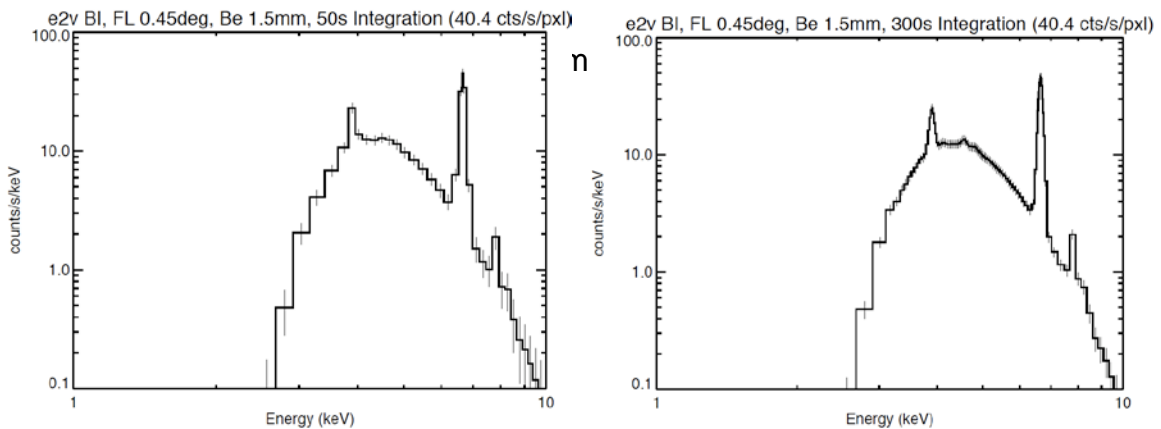


Figure 4.14. Simulated photon count spectra for a model flare of GOES M2 class with the photon-counting mode of the telescope of $\theta_i = 0.45^\circ$. *Left*: Net integration time 133 s. *Right*: Net integration time 800 s. 1.5 mm-thick Be filter assumed as the attenuation filter so that the incident photon count rate to the detector reduced to 40.4 counts/s/pixel.

Based on the above observation capability for active regions and flares, imaging-spectroscopic performance of the photon-counting telescope is schematically illustrated in Figure 4.15. The figure presents angular size (in arcsec) of observation target versus temporal resolution that can be attained with the baseline photon-counting telescope. (Here, 'baseline' refers to instrument capability summarized in Table 4.2 and 4.4.) Lower-left direction in the figure corresponds to smaller target (angular resolution) with higher temporal cadence hence preferable for observations. For performing

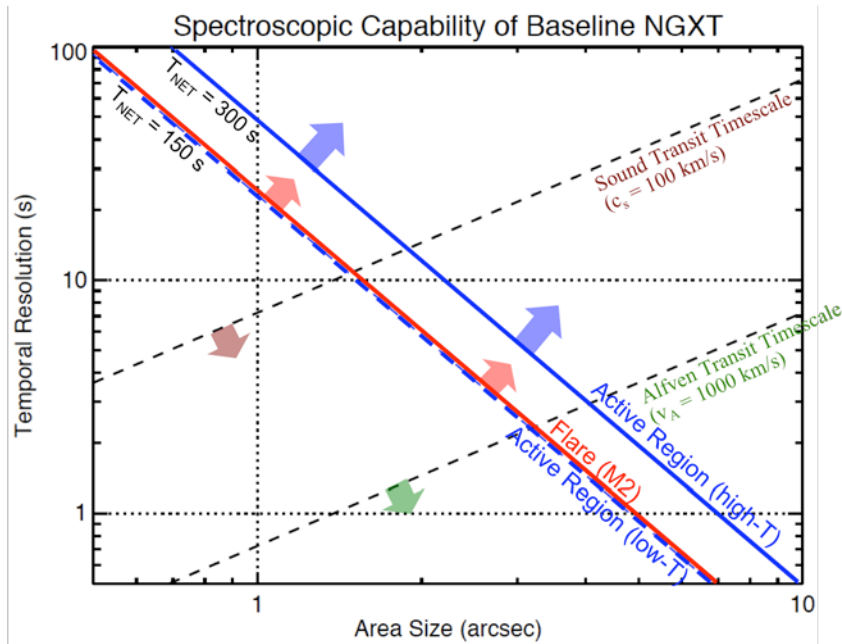


Figure 4.15. Imaging-spectroscopic capability expected for the baseline photon-counting telescope. See text for details.

imaging-spectroscopy on high temperature emission in the range of 1-2 keV, upper-right side region from the solid blue line (with label 'Active Region (high-T)') can be addressed by the instrument, while angular size-temporal resolution combination in the left-side region would result in insufficient photon statistics for generating soft X-ray energy spectra. On the other hand, for imaging spectroscopy on low temperature emission in the range below 1 keV, upper-right side region from the blue dashed line (with label 'Active Region (low-T)') can be addressed.

For flare observations, the border is shown in solid red line (with label 'Flare (M2)'), and imaging-spectroscopic observations can be performed with good photon statistics for the region upper-right of the border. If we could have small charge spreading (less than 3×3 pixels), or could adopt a better event selection method (if it exists) other than the one discussed in the Appendix, the border would be further pushed down towards lower-left direction in the figure, enabling us to investigate spectroscopically smaller region with higher temporal cadence.

In Figure 4.15, two dashed lines from lower-left to upper-right, one roughly indicating sound transit time scale (with sound velocity set as $c_s = 100$ km/s) and the other Alfven transit time scale, are shown. With the baseline imaging-spectroscopic

performance of the photon-counting telescope, physical processes with sound time scale in active regions would be observed with angular resolution (size) of 2" and temporal resolution of ~10 s, while those with Alfvén time scale in flares with angular resolution (size) of ~3" and temporal resolution of ~2 s.

4.3 Ultra-High Spatial Resolution Normal Incidence EUV Telescope

As demonstrated by *Hinode* observations, activities in the lower atmosphere of the Sun, such as those of spicules in the chromosphere, and their consequences to the upper atmosphere, may hold the key to understand energy transfer and subsequent dissipation (heating) into the corona. While dynamics of the transition region and the lower corona will be extensively studied quantitatively by EUVS, combination with an imaging telescope with the following features as compared to EUVS should further enhance science output on the dynamics, energy transfer and dissipation in the transition region and the low corona.

- (1) Temperature overlap
- (2) Higher spatial resolution
- (3) Higher exposure cadence
- (4) Wider field of view

Data from *Hinode* EIS has clearly indicated that there is structure and velocity component present whose spatial scale below the instrument resolution. A similar case could happen with the EUVS instrument under which full interpretation of observed data, such as line profiles, would confront difficulty. An imaging telescope with the above-listed features should provide context information for EUVS and would greatly help to understand what is going on in their data.

As the spatial resolution of the EUVS instrument will be ~0.3" (~0.16" pixel size), that for the imaging telescope should be equal to, or better than, 0.2"-0.3" (~0.1" pixel size). The need of ultra-high spatial resolution together with temperature overlap with EUVS leads to the choice of EUV normal incidence optics.

While EUV image data should be quite useful to observe structure, motions and magnetic environment of coronal phenomena, the image data by themselves would be not suited to derive physical quantities such as density, actual temperature and velocity of coronal plasmas. Nevertheless, with the spatial resolution of 0.2"-0.3", the EUV normal incidence telescope, when combined with EUVS, is expected to contribute in Solar-C/Plan-B science in the following aspects: (1) Resolve fine, hopefully elemental, structures and study plasma flows, magneto-acoustic waves and small-scale heatings in coronal temperature range, (2) investigate transfer and dissipation mechanism of magnetic energy, and (3) understand how corona reacts to activities that occurred in the lower atmosphere. Furthermore, the movement of the localized particle-acceleration site can be also investigated by observing the EUV flare kernel with high spatial and temporal resolution (Figure 4.16).

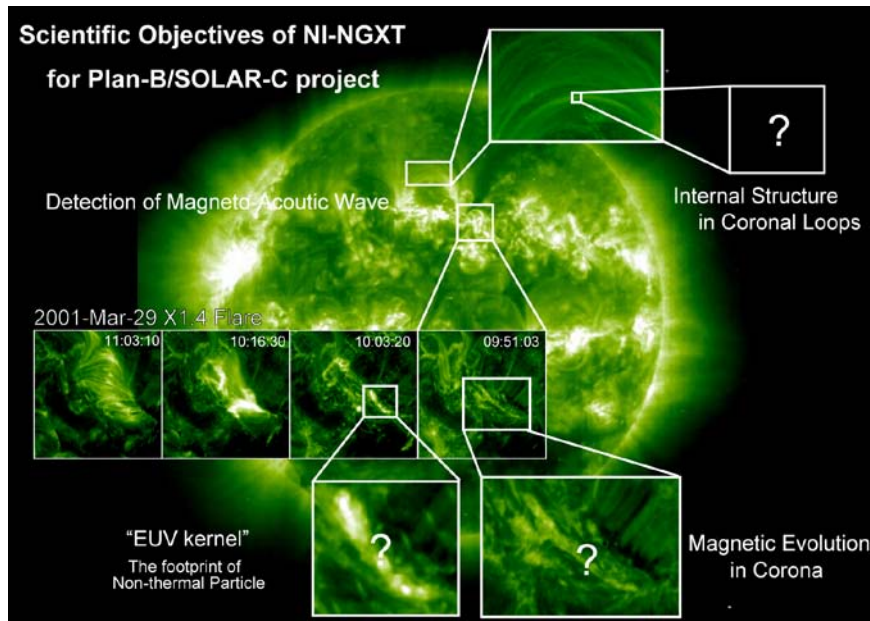


Figure 4.16. Target structures and phenomena of the ultra-high spatial resolution normal incidence EUV telescope.

4.3.1 Scientific Requirements for the Instrument

The primary goal of the ultra high-spatial resolution normal incidence EUV telescope for Solar-C/Plan-B mission is to give support in understanding physics of magnetic energy storage and release in coronal plasmas by investigating how corona reacts to activities that occurred in lower atmosphere. Based on the science goal, scientific requirements on the EUV telescope are summarized below to deliver largest synergy with EUVS.

1. The telescope should have higher angular resolution than EUVS, that is, to resolve structure with 0.2"-0.3" resolution with 0.1" detector pixel for resolving fine coronal structures to give aid in understanding elemental processes in corona.
2. Exposure cadence should exceed that for EUVS. As exposure time for EUVS is 1-5 s for active regions with 0.33" spatial sampling while that for the EUV telescope for active regions and flares can be as short as 1 s and 0.1 s, respectively, the requirement on cadence can be reasonably met.
3. Field of view should well cover that for EUVS (that is 200" nominal, >300" extended). This results in the telescope field of view requirement of ~400"×400". Note this size covers even outer structures of an active region.
4. Temperature range should well overlap that for EUVS. This could imply multiple normal-incidence channels for the telescope. The temperature overlap would also help in co-aligning image data with EUVS. A UV band for the telescope may also

be useful for co-alignment with SUVIT data.

5. To perform observations with low-scattering optics. In order to observe faint structures in the corona, such as long loops in active regions, plume in coronal holes and structures on the limb, scatter light of the telescope has to be low.

4.3.2 Strawman Instrument Concept

The following depicts preliminary, strawman instrument concept of the EUV telescope. Specifications of the instrument design should be elaborated in coordination with the EUVS instrument.

4.3.2.1 Optical design

The instrument will consist of two telescopes. The telescopes have the same optical design except the optical bandpass. The optical design of the telescope is a Ritchey-Chrétien form of Cassegrain. The primary and secondary mirrors are divided to three sectors and each sector is coated by the different multi-layer coatings for focusing in 3 different wavelengths by one optical system.

At the front aperture of each telescope, there are entrance filters and an aperture selector. The aperture selector conceals two third of the aperture and solar EUV light incidents only on one sector of the primary mirror. The light then travels the telescope tube to the primary mirror, where it is reflected back toward the secondary. The secondary is mounted on an active structure that is actuated to remove the instrument pointing errors and focus the system. Light reflects off the secondary, and toward the focal plane. There is a shutter and filter wheel near the focal plane. The shutter controls the exposure time. The filter wheel places the desired filter in the light path, thus controlling the spectral content of the incoming light. Since the mirror coatings act as narrow bandpass filters, the focal plane filters effectively select which channel of the telescope is sending light to the detector. The telescope has the guide telescope for tracking the position of the sun and measuring the instrument pointing error that is used for image stability compensation. The optical design and the guide telescope system are similar to that of the AIA/SDO and the TRACE.

4.3.2.2 Exposure time and the diameter of the primary mirror

Based on the refractivity of the mirrors, the transmission of the filters and the quantum efficiency of the CCD used in the AIA/SDO, we expected the effective areas for EUV lines of the instrument, and predicted the exposure times for accumulating 200 photons/pixel. The threshold count rate "200 photons/pixel" is needed to decrease the error of the count ratio between the X/EUV bands to less than 10%. The count ratio is useful for the temperature analysis of corona. Fig 4.17 shows an example of the results.

Recently, there has been remarkable development in CMOS active-pixel image sensors which appear to be best suited as our photon-counting detector because of their small pixel size (can easily be smaller than 10 μm) and their potential of high frame readout capability.

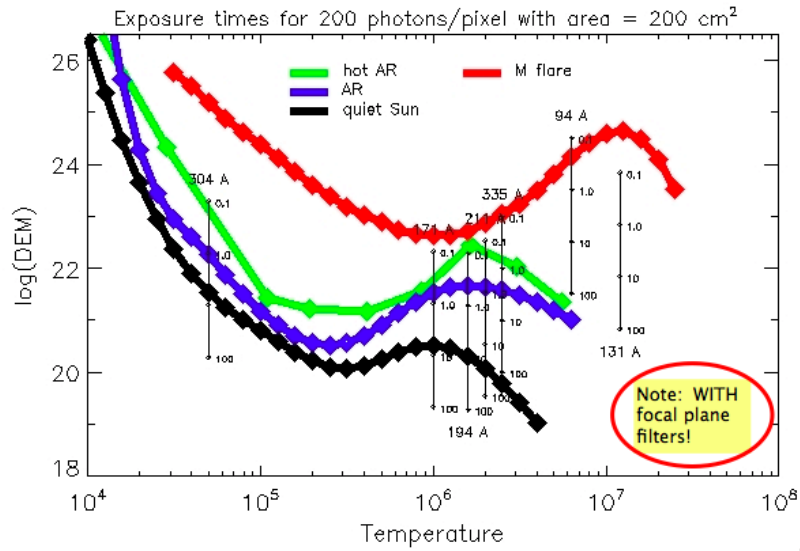


Figure 4.17. The Differential Emission Measures and the predicted exposure time for the EUV lines. The vertical bar indicates the exposure time for each EUV lines if the geometric area of the mirror for each EUV line is 200 cm^2 .

4.3.2.3 Selection of wavelength and temperature coverage

The strawman instrument has 5 narrow EUV bands and one broad UV band. In order to observe the corona with continues temperature coverage, the five EUV bands are chosen for the instrument based on our knowledge of the solar EUV image taken by the EIT/SOHO, the TRACE and the AIA/SDO.

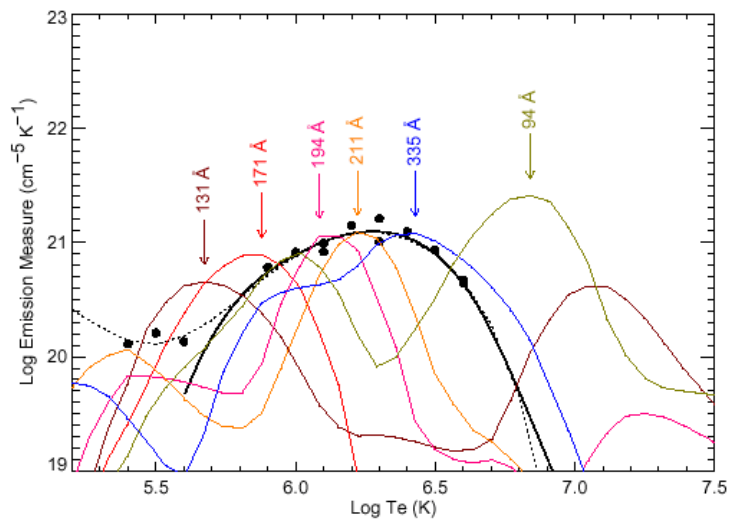


Fig 4.18. The temperature coverage of the AIA. (Adopted from the “AIA Concept Study Report” written by AIA Science Team.)

- Selected band (main EUV line) : Temperature range ($\text{Log}_{10} T$)
- 171Å (Fe IX) : ~5.9
 - 195Å (Fe XII) : ~6.1
 - 211Å (Fe XIV) : ~6.3
 - 335Å (Fe XVI) : ~6.5
 - 94Å (Fe XVIII) : ~6.9 for a flare (blended with 6.0 component.)

The selected bands include the strong EUV lines and they have already been observed with 1" spatial resolution by AIA/SDO. The UV band of the instrument is similar to the UV band of SDO and TRACE. The 1600 Å and 1700 Å continuum images are taken with the band.

Table 4.5. Scientific summary of the instrument's characteristics

Spatial Resolution	0.2"-0.3" with 0.1"/pixel
Field of View	~400" × 400"
Wavelength Bands	171 Å, 195 Å, 211 Å, 335 Å, 94 Å and broad-UV band
Exposure time	1 s for an active region 0.1 s for a flare
Cadence	< 10 s

4.3.3 Strawman design details

Details of the strawman design are shown in Table 4.6.

Table 4.6. The strawman design details of the instrument.

Telescope	Baseline or nominal value
Number of telescopes	Two telescopes
Telescope type	Ritchey-Chrétien form of Cassegrain
Length of the telescope	< 400 cm
Optical properties	32 cm aperture diameter, TBD cm focal length, TBD microns/arcsecond plate scale
Design char.	Field of view: 400"x400", Platescale: 0.1"/pixel, Detector format: 4Kx4K
Mirror coating	Multi-layer coating by Mo, Si, SiC, Y and Al for 171Å, 195Å, 211Å, 335Å, 94Å and broad UV bands.
Stabilization	The image stabilization system is constructed from the guid telescope and the tip-tilt secondary mirror.
Focus mechanism	Moves the secondary mirror. The tip-tilt secondary mirror is mounted on the focus mechanism.
Filters	Baseline or nominal value
Entrance filters for the X/EUV bands	Must block 10^{-6} of out of bandwidth radiation. The thin-metal filters made from Al or Zr.
Entrance filter for the UV band	The filters is made from the bandpass filter on MgF2
Focal plane filters	The thin-metal filters for the X/EUV bands are made from Al and Zr . The filters for the UV band are made from MgF2.
Detector	Baseline or nominal value
Detector Type	Back side illuminated CCD
Pixel size	TBD microns
Detector format	4K x 4K pixels

4.3.4 Technical feasibility for realizing the ultra-high spatial resolution

Many elements of the strawman instrument are flight-proven by AIA/SDO and TRACE. However, the instrument will have 5-6 times better spatial resolution than the existing telescopes. In order to realize such ultra-high spatial resolution of the instrument, one should further assess the following issues.

- Micro-roughness of the mirrors.
- Influence of the boundaries between different multi-layer coatings on each mirror.
- Stabilization system for the ultra-high spatial resolution.
- Vibration levels of the movable elements, especially those of the aperture selectors.
- Stray lights in the telescope tubes.
- Influence of high energy particles in the geo-synchronous orbit.

4.3.5 Further optimization for a better instrument

The optimization of the instrument design is not completed by the NGXT science group. The science goal and the requirements for the instrument should further be defined in detail in association with EUVS. Trade-off for wavelength selection should further be investigated. Number of telescopes, number of wavelength sectors on each mirror, types of multilayer coating and the diameter of the primary mirrors are closely related to this issue. The optical design may be further optimized for suitable observations of the corona in the Solar-C mission.

Appendix 4.A Event Processing

Since it is highly likely that electrons generated by an incident X-ray photon will spread over the pixel of incidence, it is indispensable to perform post-detection event processing to reconstruct correctly energy of incident photons by summing up electrons distributed over several pixels. Furthermore, since there is possibility that two photons incident to the same pixel, or to two adjacent pixels, in a single frame resulting in pulse pile-up (which then results in over-estimated X-ray energies), such pile-up should be avoided as much as possible with the post-detection event processing. As illustrated in Figure 4.3, this event processing is to be performed on digitized pixel data, namely, after analog voltage from each pixel signal is digitized with A/D conversion.

We here assume that all X-ray photons detected by the telescope generate electron clouds whose size ($3\text{-}\sigma$ diameter in Gaussian profile) less than 3 detector pixels. With this assumption, events whose signals contained within 3×3 pixel area but not extending beyond that, such as those shown in Figure 4.19(a) are to be identified as "valid events", and signals from the central 3×3 pixels collected to reconstruct the energy of *an* incident X-ray photon. Note in the right-most panel of Figure 4.19(a) represents a situation that two-photon incidence cannot be excluded in this particular case hence would result in inclusion of a pile-up event. However, as will be demonstrated later, probability of occurrence of such case is sufficiently low.

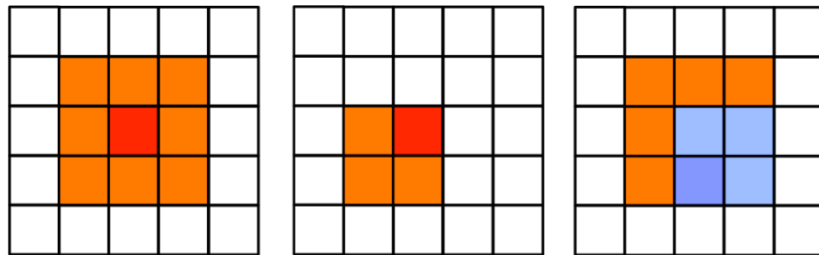


Figure 4.19(a). Example of events (indicating charge spreading across pixels) that are considered to be "valid" with 5×5 pixel-area event processing. In each panel, red pixel indicates the X-ray-incident pixel (5×5 area taken to set the red pixel at its center) while orange pixels indicate pixels with signals due to charge spreading. The right panel denotes the situation that another X-ray photon was incident (into the dark-purple pixel) in a single frame resulting in a mixture of signal charges in the 3×3 area. The right panel case cannot be excluded by the event processing.

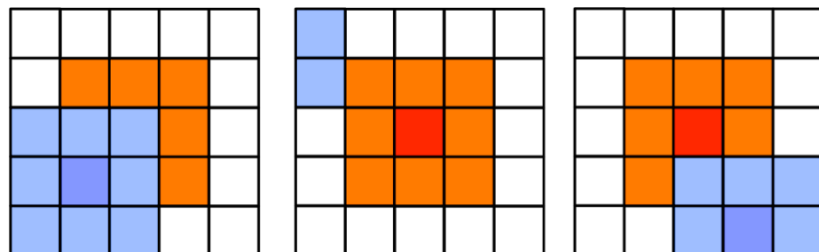


Figure 4.19(b). Example of events that are to be rejected because of possible contamination by the second photon in a frame. Pixel of the second-photon incidence is shown in dark purple with light-blue pixels denote pixels with signals from the charge spreading from the second photon. The middle panel represents a case where the second photon was incident outside the 5×5 pixel area but some of its spread charge present in the 5×5 area.

Figure 4.19(b) shows examples of "invalid events" with possibility that the central 3×3 pixel area is contaminated by charge from the second photon, due to signal distribution extending beyond the 3×3 area. Hence these events are to be rejected by the event processing.

Such post-detection event processing has been a standard technique for photon-counting CCD detectors in modern X-ray astronomy satellites such as *ASCA* and *Suzaku* (e.g., Koyama *et al.* 2007), and the same, or very similar, scheme can be applied to our photon-counting solar X-ray telescope as well. A big difference here is, however, necessary event processing speed (as determined from level of X-ray flux), is usually 1-2 orders of magnitude higher in the case of solar application than X-ray astronomy; in the latter case, a typical pixel-processing speed is ~1 Mpixels/s (Dotani, T., private communication) while the pixel-processing speed necessary for the photon-counting telescope would be 65 Mpixels/s for photon-counting area of 256×256 pixels and 262 Mpixels/s for 512×512 pixels, with 1000 fps frame readout rate. While this difference is certainly a technical challenge for realizing photon-counting imagery on the X-ray solar corona, there has been effort in the X-ray astronomy community to achieve higher-speed pixel processing for the need of observing bright celestial objects. Anabuki *et al.* (2002) reported that the pixel-processing speed of 10 Mpixels/s with 5×5 pixel-area method was achieved with an FPGA by introducing a noble pipeline scheme for processing series of pixel data. Considering technical progress in FPGAs after 2002, having pixel-processing speed of a few to ~10 times larger than this value would not be totally unrealistic. Note parallel event processing using multiple FPGA units is a viable possibility to reduce processing speed for each unit.

Now let us consider what fraction of the incident photons is detected as "valid events" by the event processing method with 5×5 pixels. Suppose average number of photon incident for each frame sample, for each pixel, is p (photons/pixel/sample). As the photon incidence events follow Poisson statistics, the probability P_{tot} of having a valid event (which contains cases such as the right panel of Figure 4.19(a)) is given by

$$P_{tot} = (1 - e^{-p}) \times e^{-24p}.$$

This probability includes cases of, not only pure single event, but also multiple events (pile-up events) whose charge distribution happened to be contained in a single 3×3 pixel area. Since the single-event probability P_1 for the central pixel is expressed as

$$P_1 = p \times e^{-25p},$$

ratio of single events among detected valid events R_1 is

$$R_1 = \frac{P_1}{P_{tot}} = \frac{p}{e^p - 1}.$$

Figure 4.20 presents P_{tot} , P_1 , and R_1 as a function of p . P_{tot} takes the maximum value of 0.015 at $p = 0.041$ photons/pixel/sample. This means, with $N = 1000$ fps frame readout, 15.0 counts/s/pixel is detected as valid events out of photon incidence rate of 41 counts/s/pixel. Single-event fraction R_1 exceeds 90% for $p \leq 0.2$ photons/pixel/sample. Figure 4.21 shows valid-event detection rate, in terms of counts/s/pixel (*i.e.*, in every seconds, instead of every sample) as function of average photon incidence rate to the detector (in terms of photons/s/pixel) and frame readout rate (fps). Obviously, fraction of valid events against incident photons decreases as the incident photon rate increases, because of increased probability of multiple photon incidence in a single

frame. This is an important aspect of photon-counting observations that excessive incident photon rate simply results in few number of single-events that are useful for generating energy spectra. Namely, the incident photon count rate has to be adjusted to an appropriate level so as to have good number of single-events detections.

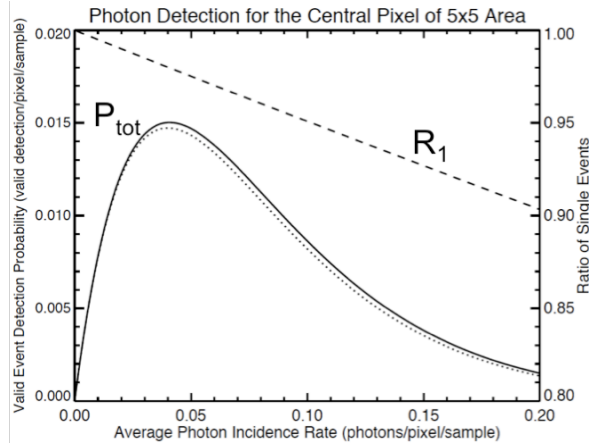


Figure 4.20. Profiles of valid-event detection probability P_{tot} (solid curve) and single-event fraction R_1 as function of average photon count rate p (photons/pixel/sample). Scales on the left Y axis apply to P_{tot} while those on the right Y axis to R_1 . Probability of being a single event (P_1) is also shown in the figure as a dotted curve.

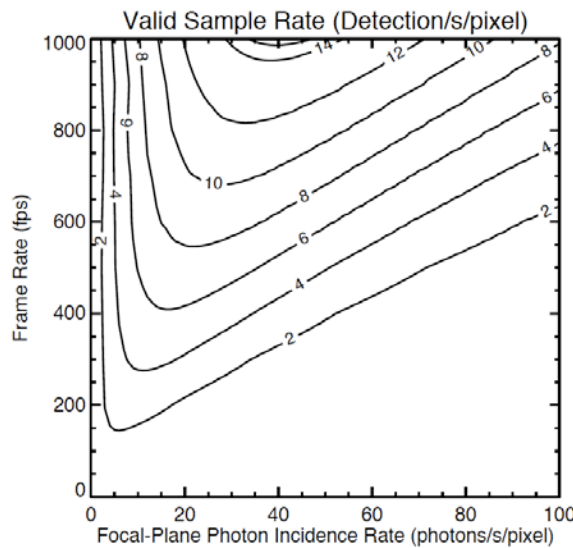


Figure 4.21. Valid-event detection rate (in terms of counts/s/pixel) with respect to average photon count (incidence) rate (photons/s/pixel) and frame readout rate (fps). Profile of P_{tot} in Figure 6.A-2 corresponds to a horizontal cut at the frame rate of 1000 fps in this figure.